Chemical assembly of nanostructured films for sensing applications

Xiaogang Wen, Louzhen Fan, and Shihe Yang*
Department of Chemistry, The Hong Kong University of Science and Technology, Clear Water Bay, Kowloon, Hong Kong

ABSTRACT

A series of inorganic nanorods, nanowires, nanoribbons, and nanoscrolls have been synthesized in large-area arrays vertically aligned on metallic surfaces. The simple syntheses of the nanowire films are accomplished in situ by gas-solid and liquid-solid reactions under mild conditions. For the preparation of endohedral metallofullerene films, solution casting and electrochemical techniques are employed. The structural, optical, and electrical properties of the nanostructures have been characterized, which provide interesting prospects of these film materials in various applications. Potential uses of these films as passive and/or active components in dye-sensitized solar cells and gas sensors have been demonstrated in a number of preliminary experiments.

Keywords: Nanowires, metallofullerene, films, synthesis, sensors

1. INTRODUCTION

The last decade or so has witnessed an explosive development in the synthesis of nanostructured materials, such as derivatized fullerenes, carbon nanotubes, nanoparticles, nanowires to name but a few[1]. One of the emerging issues is how to manipulate and assemble the nanostructures to introduce and realize functionalities. Apparently, the full potential of nanotechnology is represented by the ability to not only synthesize a rich variety of nanoscale building blocks but also assemble them into various patterns by design at the supramolecular and supracluster levels. In particular, the application of nanoparticle and nanowire materials often requires their assembly into the form of thin films. In this paper, we will describe two film systems prepared by rather simple chemical deposition methods. The first is the films of arrays of inorganic nanorods, nanowires, nanoribbons, and nanoscrolls aligned on metallic surfaces, which are synthesized under ambient conditions. The simple technique we use combines the preparation and assembly in one step and does away with the need of templates, extreme conditions, or demanding instrumentation, which are often required in the conventional fabrication of one-dimensional inorganic materials. Another system is the films of endohedral metallofullerenes prepared by the solution coating and electrochemical techniques. The endohedral doping affords a unique tuning of the photoactivity and electroactivity of fullerene molecules. The structural, optical, and electrical characterizations of these films have been performed, which point to possibilities in real-world applications. Some initial experimental results will be presented to illustrate the potential of the nanoscale film materials to serve as passive and/or active components in dye-sensitized solar cells and gas sensors.

2. SYNTHESIS OF INORGANIC NANOWIRE ARRAYS

During the past few years, we have synthesized a series of sulphide and oxide nanowire films with various ultrafine structures[2-5]. The films are grown in situ on electrode surfaces, where the nanowires are vertically aligned. The film growth is accomplished by gas-solid and liquid-solid reactions under mild conditions. The advantages of our methods are the simplicity, template-free, catalyst-free, large-area uniformity, and in-situ growth on electrode surfaces. In most cases, the nanowires are single crystals. In the following, some examples will be given to illustrate the methods we used for fabricating films of inorganic nanowire arrays.

2.1 Copper sulphide nanowire arrays

*chsyang@ust.hk; phone (852) 2358-7362; fax: (852) 2358-1594

Nanosensing: Materials and Devices, edited by M. Saif Islam, Achyut K. Dutta,
Proceedings of SPIE Vol. 5593 (SPIE, Bellingham, WA, 2004)
0277-786X/04/$15 · doi: 10.1117/12.570084

The copper sulphide (Cu_2S) nanowires are directly grown on copper substrates by gas-solid reactions[2]. This is accomplished simply by exposure of a copper surface to O_2 and H_2S at room temperature and ambient pressure. Immediately on exposure to the gas mixture, the copper surface became dark red, shinning cyan, and gray in a short time span. After 10 h reaction, the copper surface was covered with black and fluffy materials, indicating the formation of dense Cu_2S nanowire arrays. A typical SEM image of the as-grown Cu_2S nanowires on copper is shown in Figure 1. The nanowires are straight and circular in cross section with diameters of a few tens of nanometers. Needle-shaped nanowires can also be produced under appropriate conditions. High-resolution transmission electron microscopy (TEM) shows that the Cu_2S nanowires are single crystals of monoclinic structure, which grow along the *c*-axis. The identification of nanowire composition was accomplished by a variety of techniques including X-ray photoelectron spectroscopy, UV-Vis absorption spectroscopy [74], electron paramagnetic resonance spectroscopy, and X-ray diffraction (XRD).

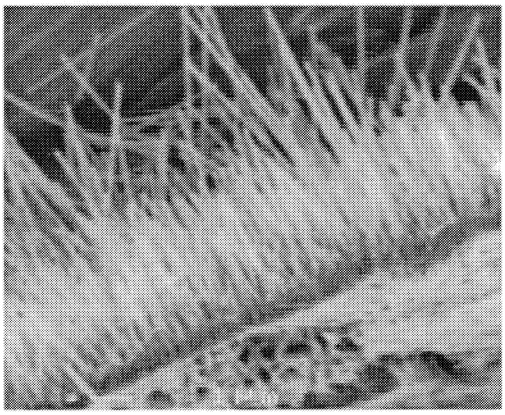

Figure 1. SEM image (side view) of a Cu_2S nanowire array grown on a copper foil by gas-solid reaction at room temperature.

Knowing that the nanowires are more or less perpendicular to the copper surface, it has been concluded that the growth direction of the Cu_2S nanowires is along the *c* axis of the monoclinic Cu_2S. This conclusion has been corroborated by high resolution TEM. In general, the Cu_2S nanowires have a uniform thickness of ~4-100 nm and a length of tens of micrometers depending on the synthetic conditions. They appear to be well-crystallized although the outer portion consists of some oxide nanoparticles.

We have identified some important effects of copper surface structure, reagent gas composition, and reaction temperature on the growth of Cu_2S nanowires. For example, the Cu_2S nanowires can only grow on certain surface of copper, i.e., Cu (220). The nanowire diameters increase with increasing temperature, and to a less extent, with increasing molar ratio of O_2 to H_2S. At high temperatures and high molar ratios O_2:H_2S, the nanowires become thicker, less uniform in diameters, coated with nanoparticles, and even evolve into nanocones or nanoneedles.

The ability to synthesize Cu_2S nanowire arrays directly on an electrode surface at room temperature has not only opened the possibility of a host of applications such as field emission displays, but also raised intriguing questions about the growth mechanism. On the basis of our experimental results, we believe that the initial stage involves the nucleation of Cu_2S nanoparticles, which then grow continuously on the top.

2.2 Copper oxide nanowire arrays

For the synthesis of CuO nanorod arrays on copper surfaces, we use liquid-solid reactions at room temperature. A typical synthesis of p-CuO nanorods was carried out as follows. First, a copper foil (1 cm^2) was washed with a 4 M HCl solution for ~15 min and subsequently with de-ionized water three times to remove surface impurities. The washed copper foil was then immediately immersed into 400 ml of water containing 1 ml of ammonia (13 M) and 2 ml of NaOH (1 M) solutions at room temperature (pH is 11 at this concentration). After a given reaction time (96 h), the sample was taken out of the solution, washed with deionized water three times, and dried in air. A black film was obtained (viewed through naked eye), which covered uniformly on the Cu substrate. The pH of the solution was varied for growing the CuO nanorods by changing the amount of NH_3 and NaOH solutions. For pH 11.5, 400 ml of water containing 2 ml of NH_3 (13 M) and 3 ml of NaOH (1 M) solution was used. Whereas for pH 12, 400 ml of water containing 1 ml of NH_3 (13 M) and

10 ml of NaOH (1 M) and for pH 12.3, 400 ml of water containing 5 ml of NH_3 (13 M) and 15 ml of NaOH (1 M) were used. Different growth times were also investigated.
Figure 2 shows an SEM image of p-CuO nanorods grown on a copper foil substrate at pH = 12.3 and reaction time = 14 days. As can be seen from the figure, the nanorods cover the copper surface uniformly, smoothly and compactly. In addition, the nanorods are roughly aligned perpendicular to the substrate surface. When the reaction time was increased from 96 to 130 h, the lengths of the nanorods were increased. Preliminary transmission electron microscopy examination showed that the CuO nanorods are about ~10 nm thick and a few hundred nanometers long. When the solution pH was varied from 11.0 to 12.3, the black nanorod film was very compact and the colorless solution became bluish, indicating the dissolution of Cu^{2+} under the strong basic condition. At pH 12, the nanorods were visibly formed within 96 h. However, when the pH was increased to 12.3, the CuO nanorod growth was much slower and in fact only visible after a period of 7 days. To cover the complete surface of the copper substrate took nearly 14 days. The observed surface of the CuO nanorod array film at this pH is somewhat shiny compared to the samples prepared under lower pHs. Also, the growth is more compact as can be seen from the SEM image.

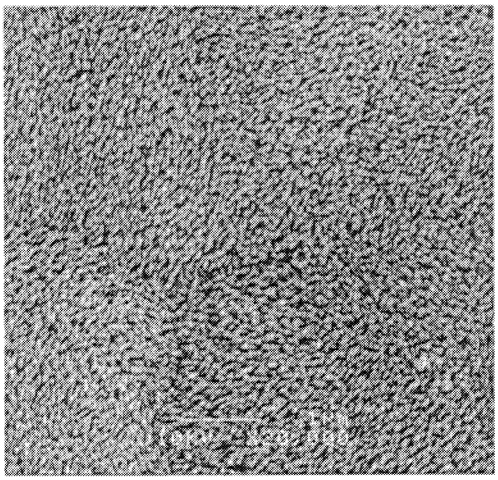

SEM image of a CuO nanorod array grown on a copper foil by liquid-solid reaction at room temperature.

The XRD pattern of the as-synthesized p-CuO nanorod/Cu samples has been analyzed. It matches quite well with the XRD diffraction data of the monoclinic CuO powder (JCPDS 45-0937). The observed peaks are similar for all the samples prepared at different pHs and growth time intervals. The chemical reactions that are involved in the room temperature growth of the CuO nanorod arrays on copper are believed to proceed as follows:

$$Cu + O_2 + H_2O + NH_3 \rightarrow Cu[NH_3]_4^{2+} \quad (1)$$
$$Cu[NH_3]_4^{2+} + 2OH^- \rightarrow Cu(OH)_2 \quad (2)$$
$$Cu(OH)_2 \rightarrow CuO + H_2O \quad (3)$$

The reactions (1) and (2) were used previously for the synthesis of $Cu(OH)_2$ nanoribbons[5]. The key difference here is that the solution used is much more basic so that $Cu(OH)_2$ is unstable and thus immediately decomposed to CuO. This is consistent with the fact that the blue color characteristic of $Cu(OH)_2$ never appeared on the copper surface during growth. As a result, we obtained an excellent adhesion of the CuO nanorods to the Cu substrates. To sum up, we have successfully synthesized CuO nanorod arrays in situ on a copper electrode. The advantages of our method for the nanorod film synthesis includes low temperature, uniform size, superior adherence, and homogeneous coverage.

2.3 Zinc oxide nanowire arrays

Two methods have been used for the synthesis of ZnO nanowire films. One is the direct growth of ZnO nanowires on Zn substrates and the other includes Zn powder deposition on a Si substrate, followed by conversion to ZnO nanowire arrays. It should be noted that both methods use thermal oxidation at several hundred degrees centigrade. So the surface of the

sensing materials is critical for the sensitivity, accuracy, repeatability and stability of the sensor. The conventional gas sensors mostly use thin film structure (2D nanostructure) to increase the surface area and reduce the dosages of the sensor materials.

ZnO nanobelt arrays were synthesized by gas-solid reaction at ~600°C in air. Zn powder (1-2 mg) with particle diameter of < 10 μm was ultrasonically dispersed in ethanol and the suspension was dropped on the surface of a low resistance Si substrate (8 x 8 mm^2, 50 Ω/square) rapidly. After ethanol evaporation in air, a gray Zn particle layer was formed uniformly. The Si-supported Zn film was then transferred into a crucible and loaded into a mantle heater. The heater was heated to 600 °C in 20 m and kept at this temperature for 6-12 h before it was cooled down to room temperature naturally in air. A white film (pure ZnO as verified by XRD analysis) was obtained, which was uniformly coated on and tightly adhered to the Si substrate.

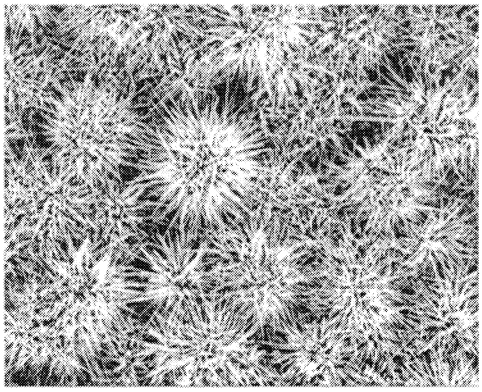

Figure 3. SEM image of a ZnO nanobelt film grown on a Si substrate by thermal oxidation of Zn particles at 600 °C.

An SEM image of the as-prepared sample is shown in Figure 3. First of all, the ZnO nanowires actually have a belt-shape. It is clear that the nanobelts are grown radially from the Zn micro particles, yielding an urchin-like morphology. This urchin-like features are assembled on the Si substrate uniformly. Notably, most of the ZnO nanobelts grow thinner from inside out with very sharp tips (~50 nm in width). TEM investigations show that the ZnO nanobelts are several tens to 300 nm in width, several to several tens μm in length and their thickness is only about several to 20 nm.

2.4 Iron oxide nanowire arrays

Vertically aligned iron oxide nanobelt and nanowire arrays have been synthesized by direct thermal oxidation of iron substrates under the flow of O_2. The effects of reactive gas pressure, composition, and temperature have been systematically studied. It was found that nanobelts (width: tens of nm; thickness: a few nm) are produced in the low-temperature region (~700 °C) whereas cylindrical nanowires tens of nm thick are formed at relatively higher temperatures (~800 °C). Both nanobelts and nanowires are single crystallites with a length of tens of μm and uniformly aligned on a large-area surface. The nanobelt and nanowire growth habits in the two temperature regions indicate the role of growth rate anisotropy and surface energy in dictating the ultimate nano-morphologies.

The thermal oxidation method was used to synthesize the α-Fe_2O_3 nanobelt and nanowire arrays. The experimental setup consists of a horizontal tube furnace of length 120 cm and diameter 10 cm, a quartz tube 100 cm in length and 5 cm in diameter, and a gas flow/control system. Iron foils (10 mm x 5 mm x 0.25 mm) with a purity of 99.9% (Aldrich) were used as both a reagent and a substrate for the growth of α-Fe_2O_3 nanowires. The iron foils were carefully cleaned with absolute ethanol in an ultrasound bath before being loaded into a quartz boat, which was positioned at the end of the quartz tube. The quartz tube was then mounted in the middle of the tube furnace. A flow of high-purity nitrogen (>99.995%) was first introduced into the quartz tube at a fast rate (~200 sccm) for 20 min. in order to remove air in the system, and then adjusted to 20 sccm accompanied by a flow of oxygen at a rate of 2-5 sccm. At this time, the tube furnace was heated up at a rate of 20 °C/min to the designated temperature. After being held at this temperature for ~10 h, the system was allowed to cool down naturally to room temperature. The product samples were then collected, which consisted of a scarlet layer homogeneously coated on the substrate. Fig. 4 shows an SEM image of the Fe_2O_3 nanowire

array prepared at 800 °C. Clearly, only wire-like features were produced, which are aligned in dense array approximately perpendicular to the substrate surface. The coverage of the array on the substrate appears to be quite uniform judging from the SEM images.

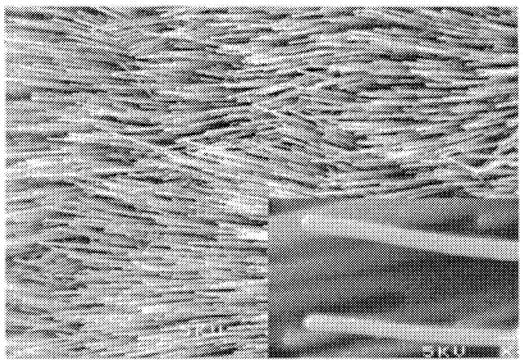

Figure 4. SEM image of an Fe_2O_3 nanowire array grown on an iron foil by thermal oxidation of iron at 800 °C.

The nanobelt morphology is also observed for samples prepared at lower temperatures. In fact, belt bending is observed on the top tips of all of the as-grown arrays. In general, the nanobelts obtained under our growth condition are about 5-10 nm in thickness, 30-300 nm in width, and 5-50 μm in length. The width and thickness of a given nanobelt is uniform along the whole length except at the top tip, where thinning and thus bending usually occur.

Temperature dependence of the nanowire growth has been studied. At 400 °C, only very little wire-like structures can be observed, which are meandering and sporadic. Instead, the surface is mainly covered with seemingly well-crystallized flake-like structures. XRD data has confirmed that the flake-like structures are pure α-Fe_2O_3. Increasing the temperature to 600 °C is accompanied by an increase of the density of the wire-like features and the extent of the alignment. However, the flake-like structures are still all-pervading. It is worth noticing that, without exception, the wire-like features are all grown out of the cleft between the protruding flakes. When temperature is increased to 700 °C, the surface of the substrate is all covered by a dense nanobelt array and no flake-like structure can be found. Finally, with a further increase of the temperature to 800 °C, the nanobelt array has evolved into an even more uniform array consisting of cylindrical nanowires (Figure 4). A distinction between the nanobelts and the nanowires lies in the winding top tips of nanobelts and the straightness of the nanowires. The cylindrical nanowires average ~30-60 nm thick and several tens of micrometers long.

The XRD patterns of both the nanobelts and the nanowires are in conformity with rhombohedral α-Fe_2O_3 (a = 5.038 Å; c = 13.772 Å). In the XRD pattern of nanobelt array, the relative peak intensities of the diffraction planes (110) and (300) are much higher when compared with the standard powder diffraction pattern of bulk α-Fe_2O_3. Preferential orientation and alignment of the nanobelt crystals on the substrate is plainly the explanation. As will be described below, the α-Fe_2O_3 nanobelts grow along the <110> direction, which gives rise to a relatively intense diffraction peak of the (110) plane. We further recall that the nanobelt top tips are generally bowed; the bending is not severe but probably to the extent that the (300) plane becomes roughly parallel to the substrate surface (<100> is at an angle of 30° with <110>). This explains why the (300) diffraction peak is even much stronger than the (110) diffraction peak. As for the nanowires, although the intensity of the (300) diffraction peak becomes comparable to that of (110), the tilting of the nanowires away from the surface normal is still indicated.

Our present studies provide some clues to the 1D growth mechanisms of α-Fe_2O_3. Some general remarks are in order. First of all, due to the very low Fe and α-Fe_2O_3 vapor pressures (the melting points of Fe and α-Fe_2O_3 are 1535 °C and 1350 °C, respectively) at the temperatures of our syntheses, the 1D growth of α-Fe_2O_3 is inexplicable by the vapor-liquid-solid (VLS) and vapor-solid (VS) mechanisms. The former is rejected by the fact that no spherical particles have been found at the tips of the nanowires and the latter is ruled out because all of the 1D features we observed were grown out of the substrates and nowhere else did we find any trace of α-Fe_2O_3 nanowires. Second, we have shown that low-temperature synthesis prefers the formation of the nanobelts and high-temperature synthesis favors the growth of the

nanowires. This nanobelt-to-nanowire morphology transition is probably related to surface energy and different growth rates along different crystal directions. Third, we have noticed that the nanobelts are all grown out of the gaps between flakes; no nanobelts were nucleated on the well-crystallized flakes. This indicates that the nanobelts grow from defects such as planar defects of twins and grain boundaries. Finally, our results tend to support the tip-growth mechanism, which was proposed by Takagi et al. With the lapse of reaction time, the narrowing and thinning of the nanobelts occurs. If a root-growth mechanism is operative the nanobelt root would appear to grow wider and wider with time. This is not expected because the diffusion of O_2 to the root region should be more restricted as the nanobelts grow longer.
Summarizing, we have successfully synthesized well-aligned hematite nanobelt and nanowire arrays on iron substrates by a simple Gas-Solid reaction process. The morphologies of the 1D nanostructures can be reasonably controlled by varying the reaction temperature and gas composition. In other words, the lower temperature supports the nanobelt growth whereas cylindrical nanowires are grown at the higher temperature. At least, some cylindrical nanowires synthesized at the higher temperature has a scroll-type structure. We have shown that the nanobelts and nanowires all grow along the [110] direction through the surface diffusion of Fe atoms or ions to the tips of the nanostructures.

3. POTENTIAL APPLICATIONS OF THE INORGANIC NANOWIRE ARRAYS

3.1 Dye-sensitized solar cells

Solar energy conversion processes have garnered much attention of late as the most attractive methods to generate useful form of alternative energy. In particular, dye-sensitized solar cells based on TiO_2 nanoparticles have reached an overall energy conversion efficiency as high as ~10%. Here, photoexctied dye molecules such as cis-di(thiocyanato)N,N'-bis(2,2'-bipyridyl-4,4'-dicarboxylic acid)-ruthenium (II) [N3 dye] anchored to the TiO_2 nanoparticle surfaces could inject electrons to the conduction band (CB) or holes to the valence band (VB). In these cells, a thin layer of Pt (Φ = 5.65 eV) coated on a conducting glass is normally as the counter electrode. It seems worthwhile to study the possibility of replacing the more expensive Pt/conducting glass electrode by our p-CuO-nanorod/Cu electrode. First, the work function of CuO is close to that of Pt (i.e., Φ = 5.3 eV). Second, p-CuO has a relatively high hole mobility (0.1 $cm^2 V^{-1} s^{-1}$). Third, the aligned CuO nanorods synthesized in situ with excellent adhesion on the copper substrate have a high surface area and may serve as convenient cathode for the dye-sensitized heterojunctions in solar photovoltaic applications.
Figure 5 shows the device configuration of typical photovoltaic devices. For the preparation of solar cells in the present investigation, the as-prepared p-CuO nanorods/Cu and the ITO (indium tin oxide) conducting glasses coated with dye-adsorbed TiO_2 nanoparticles (sheet resistance 85 Ω/square, brought from Delta Technologies Ltd., Stillwater) were used as cathodes and photoanodes, respectively. The TiO_2 coated ITO glasses prepared according to Sirimanne et al. were heated to 80°C, then immediately immersed into a dye solution [cis-di(thiocyanato)N,N'-bis(2,2'-bipyridyl-4,4'-dicarboxylic acid)-ruthenium (II), Solaronix, Germany, 3 x 10^{-4} M] in ethanol and kept overnight for the dye to adsorb on the TiO_2 surfaces. The ITO conducting glass was placed on top of the CuO nanorods/Cu electrode with iodine/iodide (1:1 weight ratio: 0.03 g of I_2 and LiI each) and 0.2 ml of Triton-X 100 sandwiched in between. The two electrodes (2 x 1 cm^2) were then clipped with an alligator clip.

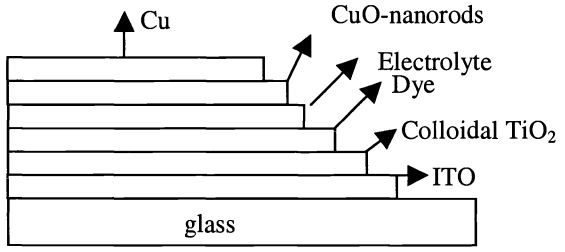

Figure 5. Schematic diagram of the device configuration.

In order to examine the device performance, the current (I) – voltage (V) characteristics of the fabricated solar cells have been measured in the dark and under illumination (15 mW/cm^2). For the [ITO/TiO_2/dye/E/CuO(nanorod)/Cu] cell (where E is electrolyte), we observed an open circuit voltage (V_{OC}) of about 564 mV, a short circuit current (I_{SC}) of about

0.450 mA, and a fill factor (FF) of 0.17 for the sample prepared under pH 12.3. Similar measurements were carried out for the other samples. In general, the I-V characteristics are similar although the detailed values may vary. It should be pointed out that these photovoltaic devices have no output potential at zero current in the dark as expected. For the sake of comparison, we also checked the solar cells with a Pt cathode, [ITO/TiO_2/dye/E/Pt/ITO], under the same illumination conditions (the Pt cathode was prepared using H_2PtCl_6). Reproducibility of the photovoltaic results presented above was confirmed by testing three such photovoltaic devices within an uncertainty of ±5%. It can be seen that the overall energy conversion efficiencies of the solar cells with the CuO nanorods/Cu cathodes, especially that prepared at pH 12.3, are not much smaller than that with the Pt cathode. This is quite encouraging given that there is still much room for improvements on the preparation of the CuO nanorods/Cu cathode.

Our photovoltaic devices take a standard configuration of dye-sensitized solar cells, where the n- and p-type semiconductor nanostructures are combined. The photocurrent mechanism is similar to that described by Tennakone et al. Upon photoexcitation, the dye molecules inject electrons to the n-TiO_2 nanoparticles network and holes to the p-CuO nanorods layer via the I^-/I_3^- redox couple. The high surface area and good hole mobility of the p-CuO nanorods contribute favorably to the photocurrent generation. However, I-V characteristics especially the fill factors (FF) still need be improved perhaps by reducing the resistance of the CuO nanorods films. Moreover, electron-hole recombination also need be alleviated by reducing interfacial trap states and by introducing new design and new material components such as blocking layers of Al_2O_3, MgO, etc.

The CuO nanorods/Cu electrode has been scrutinized as a possible candidate for the hole transporter and for the cathode in dye-sensitized solar cells based on n-TiO_2 nanoparticles. An overall energy conversion efficiency up to 0.29% has been obtained. We also show that the as-prepared CuO nanorod arrays are promising hole-transport media of dye-sensitized hetero-junctions for solar energy conversion. The possible application of these materials as cathodes of dye-sensitized photovoltaic devices has also been demonstrated. This initial result is quite promising considering that further optimization of the photovoltaic performance is possible.

3.2 Ammonia sensor

Gas sensors are very important for the environment protection and the control of reaction process, productivity, food technology, medical diagnosis, etc. A general working principle for gas sensing by a semiconductor gas sensor is based on the detection of the change of different physical parameters such as the resistance, current and capacitance etc. induced by the different reaction on the surface of the semiconductor sensor material in different gas phase. The surfaces of the sensing materials is critical for the sensitivity, accuracy, repeatability and stability of the sensor. Conventional gas sensors mostly use thin film structure (2D nanostructure) to increase the surface area and reduce the dosages of the sensor materials. Recently, companying the rapid development in the nanomaterials synthesis and application studies, zero and one dimensional nanomaterials show a remarkable advantage in forming high sensitivity gas sensor due to their much larger surface area than conventional bulk and film materials.

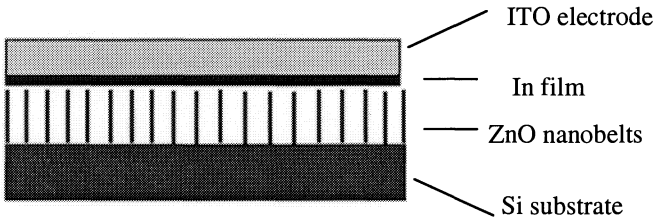

Figure 6. Schematic diagram of the device configuration.

For sensing ammonia, the ZnO nanobelt array films were directly used. The Si substrate was used as one of the electrodes and another electrode was formed by pressing an ITO slide gently on the ZnO layer. To improve the electric contact between the ZnO nanobelts and the ITO electrode, a thin, soft In film was used as a buffer layer (see Figure 6). I-V characteristics of a pure ZnO nanobelt sensor in air and in the presence of ammonia (500-1000 ppm) have been studied. The device is nearly insensitive to air, whereas the sensitivity to NH_3 increases sharply with the increasing bias voltage when $V > 2$ V. The sensor is highly stable and repeatable. The results indicate the sensor is quite sensitive to the ammonia with a maximum sensitivity of 3.4 for 500 ppm of NH_3 at room temperature. The sensor response reaches 80%

of the maximum sensitivity in about 2 min after introduction of NH_3. When the gas is switched to air, the response decays to 20% of the maximum sensitivity in about 30 s. It appears that the response speed of the sensor is reasonably good. In addition, control experiments indicate the effect of humidity on the current change is negligible.

3.3 Town-gas sensor

The combination of a ZnO nanobelt film and a CuO nanorod film was used for sensing town gas. The two films are allowed to overlap and gently pressed to make a sensor (see Figure 7). The Si and Cu substrates are then used as the electrodes. Preliminary measurements have been performed on the sensor device in term of the current increase ΔI after introduction of town gas as a function of the forward bias voltage V (CuO^+, ZnO^-; $\Delta I = I_{gas} - I_{air}$, I_{gas} is the current with town gas and I_{air} in air). The current difference increases markedly when applied voltage is higher than 3 V and when the voltage is increased to 5 V, the current difference reaches about 118 μA for 50,000 ppm town gas. Control experiments have also been done. Neither the pure ZnO nanobelt film nor the pure CuO nanorod film alone is sensitive to town gas, whereas the combination of the ZnO nanobelt film and the CuO nanorod film displays an increasing sensitivity to town gas with the increasing bias voltage for V > 2.5 V.

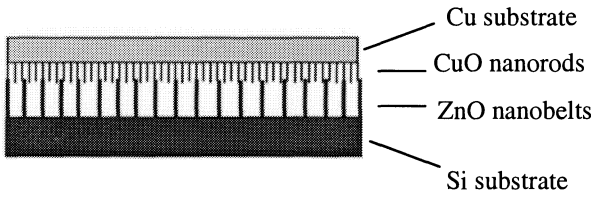

Figure 7. Schematic diagram of the device configuration.

Comparing with conventional semiconductor gas sensor which are usually operated at relatively high temperature[6-9], the nanowire gas sensors described above exhibit high sensitivity and excellent stability at room temperature. Our results show the possibility to reduce the operation temperature by using nanostructured materials as a sensing element, and fabricate room temperature or even lower temperature gas sensors, which will be very important in reducing the energy consumption and in practical applications.

4. ENDOHEDRAL METALLOFULLERENE FILMS AND THEIR ELECTROCHEMISTRY

4.1 Electrochemistry of metallofullerene films in organic solutions

One of the most intriguing properties of endohedral metallofullerenes is the electrochemistry associated with their novel electronic and supramolecular structures. The redox properties of dissolved metallofullerenes are significantly different from those of empty fullerenes. We have studied the electron transfer of $Dy@C_{82}(I)$ film on electrode surfaces in an organic solution, e.g., acetonitrile. Figure 8a displays a typical cyclic voltammogram (CV) of a $Dy@C_{82}(I)$ film on Pt electrode in acetonitrile containing $TBAPF_6$. Several pronounced redox peaks are observed and highly reproducible, suggesting that the metallofullerenes on the electrode are electroactive in the organic solution. This is in contrast to the case of the $La@C_{82}$ film in water[10], where electron transfer is obstructed. As shown in Figure 8b, the first and second reduction waves appear at –0.47 V and –1.33 V (vs. Ag/AgCl), respectively. These values are to be compared with the corresponding solution reduction waves at –0.14 V and –0.85 V (vs. Ag/AgCl), respectively (see Figure 8a). When the potential scan is reversed toward the positive direction, large splittings between the reduction and reoxidation waves for the first and the second electron-transfer reactions are observed. This is very similar to the redox behavior of C_{60} film[11-13], although the wave splittings for the $Dy@C_{82}(I)$ film are larger than for C_{60} film (the first reduction wave: 0.8 V vs. 0.5 V; the second reduction wave: 1.3 V vs. 0.2 V). In contrast to the C_{60} film, however, an oxidation wave is observed during the subsequent positive scan and a cathodic wave associated with this oxidation wave appears upon further potential scan reversal to the negative direction. Interestingly, the potential separation between these anodic and cathodic peaks is 50 mV, which is in good agreement with the characteristic value of 59 mV for a reversible one-electron transfer.

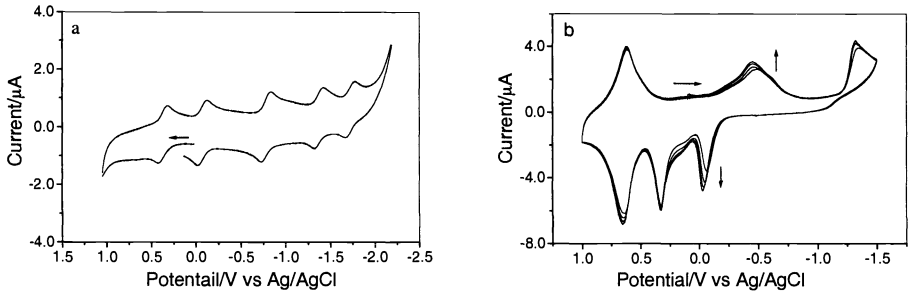

Figure 8. CVs of 1×10^{-4} mol/L Dy@C_{82}(I) in toluene/acetonitrile solution (volume ratio = 4:1) containing 0.1 mol/L $TBAPF_6$ (a) and Dy@C_{82}(I) film in acetonitrile solution of 0.1 mol/L $TBAPF_6$ (b). Scan rate = 50 $mV{\cdot}s^{-1}$.

From these results, it is clear that a peculiar structure of the Dy@C_{82}(I) film after reoxidation of the reduced film is somehow responsible for the reversible oxidation of the film. Such a structurally reorganized neutral Dy@C_{82}(I) film is oxidized and rereduced on the electrode accompanied by the incorporation of PF_6^- ions into the film on the positive sweep and the expulsion of the same ions on the subsequent negative sweep in a reversible fashion, giving rise to a very small splitting value between the oxidation and rereduction waves. The proposed mechanism for the electrode processes is illustrated as follows:

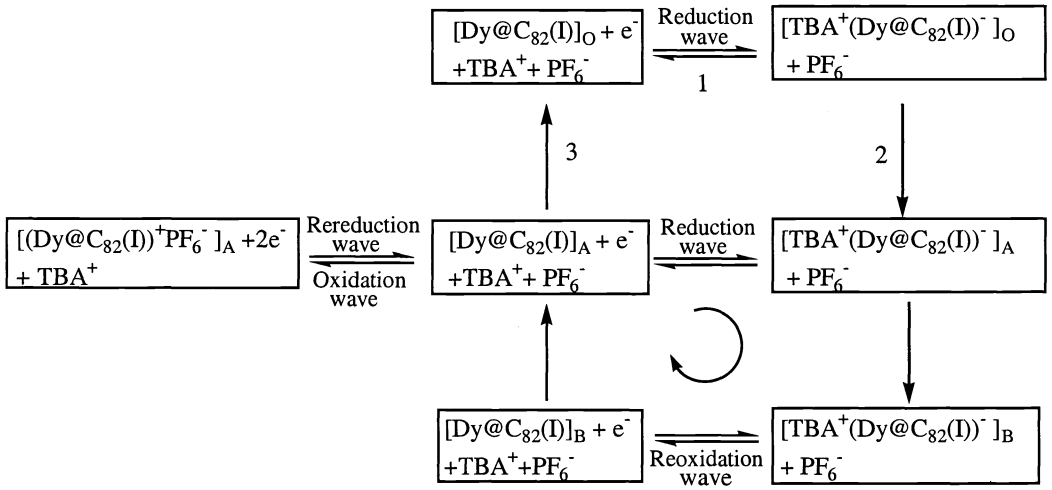

Similar to what was posited for C_{60} films, we also attribute the large splittings between the first two pairs of the reduction/reoxidation waves of the Dy@C_{82}(I) film to the attendant structural reorganization of the film due to the accommodation of the bulky TBA^+ ions for charge balance. Note that the subscripts O, A, and B represent three different structural forms of the Dy@C_{82}(I) film: O denotes the original sample, B is a structurally modified form, and A is somewhere between O and A. More specifically, as [Dy@C_{82}(I)(film)]$_O$ is reduced to [Dy@C_{82}(I)$^-$(film)]$_O$, TBA^+ diffuses towards it to form [TBA^+Dy@C_{82}(I)$^-$]$_O$ (*1*). Because of the large size of TBA^+, its intercalation requires a structural reorganization of the metallofullerene film to an intermediate structure [TBA^+Dy@C_{82}(I)$^-$]$_A$ (*2*), and all the way to the stable intercalation structure [TBA^+Dy@C_{82}(I)$^-$]$_B$. Once this is completed, the potential cycling will follow the path indicated by the curved arrow as well as that of the oxidation/rereduction waves. This explains the large negative shift of the wave1 from the first to the subsequent scan cycles, and the large splittings of the reduction/reoxidation waves.

The reorganized structure B is believed to be more open and accessible to TBA^+ so that the stable, charge-balanced ion pairs can be formed. After the reoxidation, the system enters an intermediate structure A, which accompanies the expulsion of TBA^+. Although somewhat relaxed from B, A is probably still quite open. Because PF_6^- is much smaller than TBA^+, it can easily get into and out of the intermediate structure A. In this case, the fast transport of the counter ions is perhaps assisted by solvent molecules trapped in the pores of the film. As such, no structural reorganization is needed after the oxidation/rereduction of the film, hence a small splitting of the pair is obtained. In addition, the cycling indicated by the curved arrow is necessary for the reversible oxidation/rereduction because otherwise A may change slowly to O following the path *3*.

Structural information of the metallofullerene films has also been obtained from SEM images. Figure 9 displays the SEM images of a $Dy@C_{82}(I)$ film on a Pt electrode before and after different electrochemical potential scans. The freshly coated film consists of small metallofullerene grains (<100 nm) with a uniform distribution (Figure 9a). Such a grain structure may be amenable to structural reorganization and to intercalation by foreign molecules. After electrochemical treatments, the $Dy@C_{82}(I)$ grain sizes on the electrode increase dramatically to the submicron and micron scales (Figures 9b and 9c). This is consistent with what was reported for the C_{60} film[14], and confirms the structural reorganization of the metallofullerene films. Although the details need further investigation, one may speculate that the structural reorganization involve the release of the solvent molecules trapped during evaporation and solvent-induced migration of the molecular species in the film. This would result in more open structures and consequently larger grain sizes as observed, which are then more accessible to the counter ions. It is noticed that the film images are relatively insensitive to the detailed procedures of the electrochemical treatment. For instance, the two films in Figures 9b and 9c are very similar in morphology; one has experienced the first two reduction and reoxidation waves while the other has been subjected to only the first oxidation and rereduction waves.

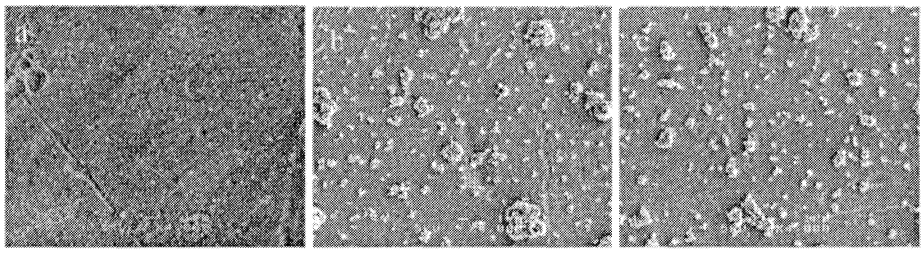

Figure 9. SEM images of $Dy@C_{82}(I)$ films. (a) Fresh film; (b) Film after reduction; (c) Film after reoxidation.

The electrochemistry of the metallofullerene film is quite different from that of the dissolved $Dy@C_{82}(I)$. Its reduction behavior is similar to that of empty fullerene film[11-13], i.e., there are large splittings between the first two pairs of reduction and reoxidation waves. However, a pair of reversible oxidation and rereduction waves has been observed. We have exploited the unique, compatible redox properties of the couple for the synthesis of a hybrid thin film of endohedral metallofullerene ($Dy@C_{82}$ is used here) and polythiophene. The deposition of the composite film of $Dy@C_{82}$/PT was accomplished by sweeping the potential between 0.0 V and 1.1 V. The electrochemical polymerization of thiophene took place on the working electrode (a Pt disk) covered with a solution cast $Dy@C_{82}$ film. Shown in Figure 10 are CVs obtained during the polymerization processes that accompany the potential sweeps.

The first CV in this figure shows that the oxidation of thiophene starts at about 1.0 V (vs. Ag/AgCl), which is the potential region corresponding to the formation of PT (see also the inset of Figure 10)[15]. Concurrently, a cathodic wave appears in the cathodic scan (+0.6 V vs. Ag/AgCl), indicating that electrodeposition has started during the positive scan. Repeated potential cycling is followed by the enhancement and slight negative shifts of the cathodic peak at ~+0.6 V, which corresponds to the reduction of the freshly deposited PT film. At the same time, an anodic peak at +0.82 V, which corresponds to the oxidation of the freshly deposited PT, emerges and continually increases and shifts slightly in the positive direction. The increases of the redox wave currents indicate the continuous deposition of PT on the electrode during the potential sweeping. In principle, increasing the concentration of thiophene and extending the potential scan range shall increase the electrodeposition rate of PT. However, too high a PT deposition rate may deteriorate the uniformity of the $Dy@C_{82}$ incorporation into the PT matrix. The potential scan rate also affects the film deposition. In

our experiments, we chose a thiophene concentration of 0.1 M, potential scan range of 0.0-1.1 V, and a scan rate of 50 mV/s. Under this condition, a light brown film started to appear after 4-5 potential sweeps, and the color of the film changed from light brown, brown, to black with the further increase of the film thickness. The thickness of the $Dy@C_{82}$/PT film could be controlled by the number of potential sweeps. The redox waves at around +0.5 V can be ascribed to the oxidation and rereduction of $Dy@C_{82}$ on the surface of the electrode[16]. It is seen that the current increases at the beginning of the potential sweeps and then becomes roughly constant after about 20 cycles. This indicates electrochemical reactions of $Dy@C_{82}$ on the electrode. Further potential sweeps are accompanied by only the increase of the currents for the doping/dedoping waves of PT. At this stage, a deep brown film is formed.

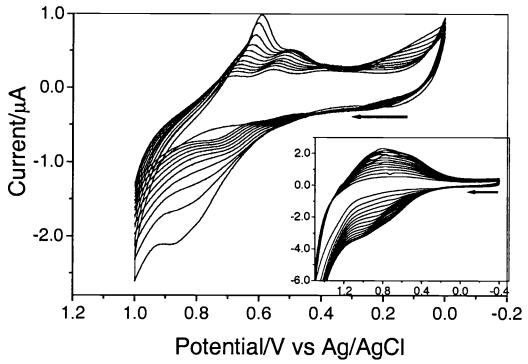

Figure 10. CVs showing PT electrodeposition on a Pt electrode covered with a solution cast $Dy@C_{82}$ film ([thiophene] = 0.1 M). The inset shows the CVs under the same condition but in the absence of $Dy@C_{82}$. Electrolyte: 0.1 M $TBAPF_6$ in MeCN; scan rate: 50 mV/s.

The electrochemical response of the resulting $Dy@C_{82}$/polythiophene film resembles that of $Dy@C_{82}$ in organic solvents with some shifts of the potential peaks, but is markedly different from that of a pure metallofullerene solid film on an electrode. Both the polythiophene backbones and the $Dy@C_{82}$ moieties appear to retain their individual electrochemical properties in the hybrid film. UV-vis and FTIR absorption spectroscopy, time-of-flight secondary ion mass spectrometry (TOF-SIMS), and scanning electron microscopy (SEM) have also been used to characterize the films. The data suggest that the $Dy@C_{82}$ molecules have been uniformly dispersed in the polythiophene matrix, forming a compact film. The formation and the electrochemical response of the hybrid film have been systematically studied, refining the viable strategy for the successful encapsulation of metallofullerenes into conducting polymers.

4.2 Electrochemistry of metallofullerene films in aqueous solutions

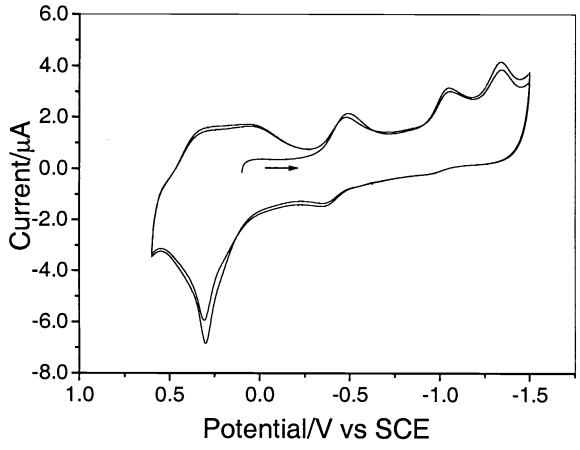

Figure 11. CVs of $Dy@C_{82}$ film on GC electrode in an aqueous solution of 0.1 mol/L TBABr. Scan rate = 50 mV/L.

In view of the promising application potentials of metallofullerenes in the biological area, it is important to scrutinize the electrochemistry of $Dy@C_{82}$ films in aqueous solution. Toward this end, we have prepared $Dy@C_{82}$ films on a GC electrode by direct solution cast and studied their electrochemical response. Typical CVs for the cast $Dy@C_{82}$ film on GC electrode in the aqueous solution of 0.1 M TBABr are shown in Figure 11. The electrochemical responses are similar to that of metallofullerenes dissolved in organic solvents with a Pt working electrode, but very different from that of the same film in acetonitrile containing 0.1 M $TBAPF_6$ with large redox peak splittings[16]. The cathodic waves at 0.040, -0.40, -1.04, and -1.35 V are ascribed the first, second, third, and fourth reduction states of $Dy@C_{82}$, respectively. The anodic wave at +0.31 V with a relatively large current is tentatively attributed to the first oxidation state as well as the reoxidation of the first reduction state of $Dy@C_{82}$. The film was found to be stable in the presence of the aqueous electrolyte solution containing TBABr. Continuous scanning over the first four reduction and the first oxidation waves for 2 h at a scan rate of 50 mV/s showed only very small changes in peak currents. Even when the positive scan was beyond the first oxidation wave so that Br^- could be oxidized, the film was still stable. It is only when the scan was beyond the fourth reduction wave that the film became less stable.

Figure 12 shows SEM images of the $Dy@C_{82}$ film on ITO before (a) and after (b) electrochemical scans in water containing 0.1 M TBABr and KCl. Before electrochemical scans, $Dy@C_{82}$ on ITO was in the form of small rod-shaped crystals, which average ~2 μm in length and ~500 nm in diameter (see Figure 12a). This morphology is very different from the aggregate form when dispersed on a Pt plate[16]. After repeated potential scans between 0.8 V and -1.5 V for several cycles in an aqueous solution of TBABr or KCl and rinses with water several times, the SEM images of the film appeared very differently. The particles became spherical and smaller (~500 nm) but still crystalline and relatively uniform (see Figure 12b). From the SEM images of the film recorded after potential scans in the TBABr-based and KCl-based electrolytes, the size of the former (~500 nm) is larger than that of latter (~250 nm), indicating that the solvation/desolvation, counter ion diffusion, and structure relaxation processes accompanying the electrochemical reactions in different supporting electrolyte solution might be different. This may be taken as possible evidence for the formation of the solvation layer as mentioned above. In fact, as already mentioned above, the $Dy@C_{82}$ films that were initially hydrophobic in the neutral form became very hydrophilic after the electrochemical reactions in aqueous solution. For example, they were no longer soluble in toluene and could be only removed from the surface by mechanical polishing. Further studies are needed to better understand the nature of the solvation layer.

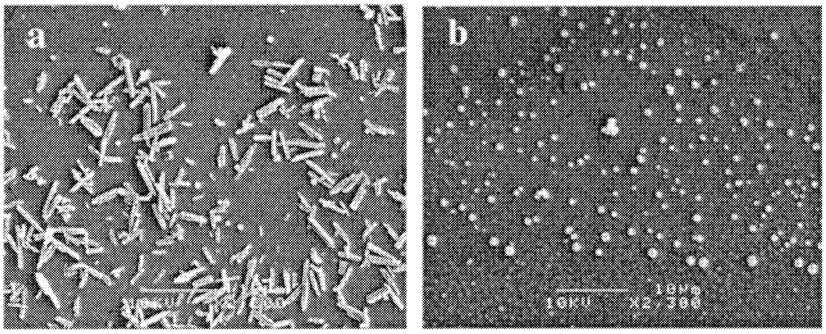

Figure 12. SEM images of $Dy@C_{82}$ film in an aqueous solution of 0.1 mol/L TBABr before (a) and after (b) cyclic voltammetric scanning.

4.3 Electrochemistry of metallofullerene films in membranes

We have also encapsulated $Dy@C_{82}$ in membrane films formed with a cationic surfactant didodecyldimethylammonium bromide (DDAB). The electrochemistry of this electrode in the absence and presence of hemoglobin (Hb) has been systematically studied. Such a protein-loaded biomembrane film may provide a good model for the understanding of redox processes in biological systems[17-19]. Typical CVs of the GC/$Dy@C_{82}$-DDAB-film/KCl (0.1 M in water) system are shown in Fig. 13a. The most prominent feature is the well-defined redox response similar to that of $Dy@C_{82}$ in organic solvents. The cathodic peaks at +0.15 V, -0.57 V, -1.12 V, and -1.39 V are assigned to the first, second, third, and fourth reductions of $Dy@C_{82}$, while the anodic peak at +0.43 V corresponds to the coalescent waves of its first oxidation and

the reoxidation associated with the first reduction. In addition, as shown in Figure 13b, repeated potential scans in the range of -0.70 V and +0.60 V show that $Dy@C_{82}^-$, $Dy@C_{82}^{2-}$, and $Dy@C_{82}^+$ are stable in the DDAB film with aqueous electrolytes. Even when the potential scanning range is broadened to 0.8 V and -1.5 V, the $Dy@C_{82}$-DDAB film is still stable with no significant decrease in cathodic or anodic peak currents. It appears that the DDAB surfactant provides a favorable microenvironment on the electrode surface for $Dy@C_{82}$, which enhances the electron-transfer rate between the metallofullerene and the electrode. The measurement of i_p vs. scan-rate exhibits a diffusion-controlled electrode process in much the same way as found by Nakashima et al. for a similar system[10].

It is important to notice that the above results were obtained in an aqueous solution of KCl. This is intriguing when one recalls that for the pure $Dy@C_{82}$ film described above, similar responses could be observed only in the TBABr solution. The redox behavior of $Dy@C_{82}$ in the DDAB membrane seems to be independent of the nature and the size of the cations in the electrolyte solution. This may be explained by the fact that the membrane molecules of DDAB (didodecyldimethylammonium ion) are already cations by themselves with a large size, which could easily balance the negative charge of the electrogenerated $Dy@C_{82}$ anions. This deduction was attested by XPS, which failed to show any K signal (K2p, 291-295 eV) in the $Dy@C_{82}$-DDAB film after potential scans in a 0.1 M KCl solution between 0.8 V and -1.6 V. As expected, however, the XPS analysis revealed the presence of Cl in this film (Cl2p, 197.5 eV). This demonstrates that the metallofullerene anions are balanced by the built-in DDAB cations while the metallofullerene cations have to be balanced by the diffusive permeation of the anions from the electrolyte solution to the DDAB membrane.

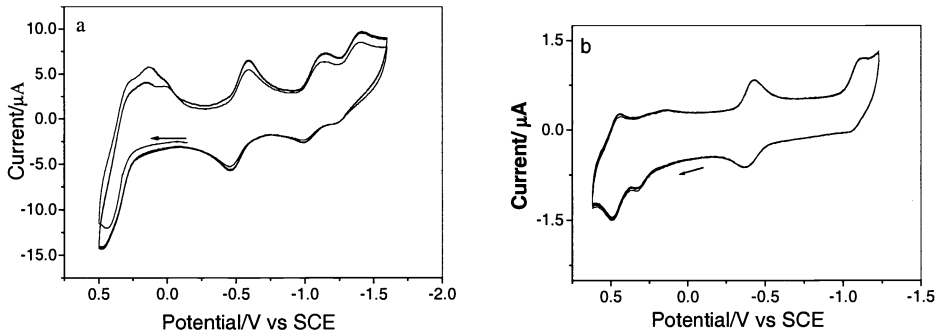

Figure 13. CVs of $Dy@C_{82}$/DDAB film on GC electrode in an aqueous solution of 0.1 mol/L KCl (scan rate = 50 mV/s). Scan range: (a) +0.5 V and -1.6 V; (b) +0.5 V and -0.7 V.

In order to better understand the redox nature of the Hb-$Dy@C_{82}$-DDAB film and explore its application potential, we have tested the electrocatalytic properties of this film through the reduction of oxygen present in the electrolyte solution. The amount of oxygen in the solution was controlled by injecting a known volume of air into the solution with a syringe. The CV data are presented in Figure 14. For the DDAB film without Hb (100 ml air), the peak at about -0.55 V reflects the direct reduction of oxygen whereas the less negative potential peak (-0.25 V) is from the reduction inside the membrane (curve *a*). The loading of Hb resulted in an increase of the reduction peak at -0.26 V with the same amount of air (curve *b*); this increase was accompanied by the disappearance of the reoxidation peak for HbFe(II). Evidently, an electrocatalytic reduction of O_2 has taken place in good agreement with previous reports[20,21]. When the Hb-$Dy@C_{82}$-DDAB film was used under otherwise the same conditions, however, a much higher reduction peak at -0.26 V was obtained (see curve *c* and *d*). Moreover, the reduction peak at -0.26 V increases with the increasing amount of O_2 in the solution (see the inset). With 100 ml of air in the cell, the peak for the Hb-$Dy@C_{82}$-DDAB film (curve *d*) is ~2.5 times higher than that for the Hb-DDAB film (curve *b*). This may be in part associated with the increased amount of Hb in $Dy@C_{82}$-DDAB as compared with that in DDAB. Another cause for the peak enhancement may be the facilitated electron transfer mediated by $Dy@C_{82}$. Although the electrocatalytic peak currents for both the Hb-$Dy@C_{82}$-DDAB and the Hb-DDAB films are linearly proportional to the amount of O_2 in the solutions, the slope of the former is much larger than that of the latter. In the dilute O_2 limit, this means that the electrocatalytic efficiency is enhanced by the encapsulation of $Dy@C_{82}$.

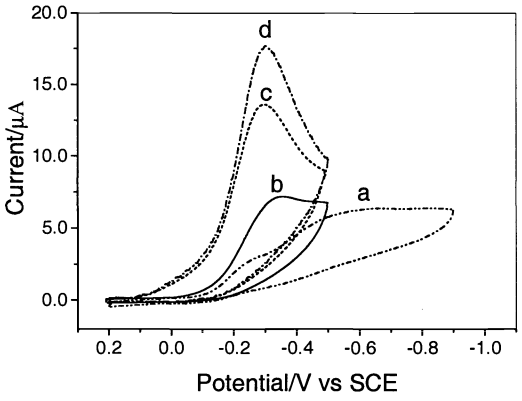

Figure 14. CVs (pH 7.0; 0.1 M KCl; scan rate = 50 mV/s. (a) DDAB film with 100 ml air, (b) Hb-DDAB film with 100 ml air, (c) Hb-Dy@C_{82}-DDAB film with 80 ml air, and (d) Hb-Dy@C_{82}-DDAB film with 100 ml air.

It is noticed that in Figure 14, the onset potential for the reduction of oxygen for the Hb-Dy@C_{82}-DDAB film (+0.18 V) is more positive than that for the Hb-DDAB film (-0.02 V), a feature which may be advantageous for low-voltage detection of O_2. In addition, the reduction peak for the former is wider than that of the latter. This is possibly caused by the reduction of more than one species at slightly different potentials. For instance, the reduction reaction may involve the electron transfer from Hb to Dy@C_{82} and then to O_2, in which the role of Dy@C_{82} as an electron transfer mediator is evident. Taken together, a possible mechanism for the electrocatalytic reaction can be expressed as follows:

$$HbFe(III) + e^- \Leftrightarrow HbFe(II)$$
$$HbFe(II) + Dy@C_{82} \rightarrow HbFe(III) + Dy@C_{82}^-$$
$$4Dy@C_{82}^- + O_2 + 2H_2O \rightarrow 4Dy@C_{82} + 4OH^-$$

Therefore, the metallofullerene molecule Dy@C_{82} can indeed serve as an electron transfer mediator for biochemical sensing.

5. CONCLUSIONS

In summary, by using very simple gas-solid and liquid-solid reactions, we have been able to fabricate nanowire arrays of a number of important sulphide and oxide materials. The nanowire growth can be controlled by the reaction conditions. The fabrication methods are low-cost, energy efficient, and easy to scale-up. More importantly, the inorganic nanowire array films can be used directly as field electron emitters, cathodes for dye-sensitized solar cells, and gas sensors. We have demonstrated the use of the oxide nanowire array films as ammonia and town gas sensors. Therefore future applications of the inorganic nanowire array films in various areas are anticipated.

The electrochemistry of metallofullerene films in both organic and aqueous solutions has been systematically studied. We have investigated the aqueous electrochemistry of bare Dy@C_{82} films and membrane films of didodecyldimethylammonium bromide (DDAB) encapsulated with Dy@C_{82}. It was found that Dy@C_{82} in the DDAB membrane promotes the encapsulation of hemoglobin (Hb) and Hb can catalyze the reduction of Dy@C_{82}. Significantly enhanced electrocatalytic reduction of O_2 by Hb in the presence of Dy@C_{82} has also been demonstrated. Here Dy@C_{82} acts an electron-transfer mediator, which points to the potential application of metallofullerenes in biochemical sensing.

6. ACKKNOWLEDGMENTS

Supports from Research Grant Council (RGC) administered by the UGC of Hong Kong and the Hong Kong University of Science and Technology are acknowledged. The authors wish to thank S. Anandan, Qiudi Liu, and Gavin Wan for their helps on some of the experiments reported here.

7. REFERENCES

1. *Nanowires and nanobelts: Materials, Properties and Devices*, Edited by Zhong Lin Wang, Kluwer Academic/Plenum Publishers, Boston, 2003.
2. S.H. Wang and S.H. Yang, "Growth of crystalline Cu_2S nanowire arrays on copper surface: Effect of copper surface structure, reagent gas composition, and reaction temperature", *Chem. Mater.*, vol. 13, pp. 4794-4799, 2001.
3. W.X. Zhang, X.G. Wen, and S.H. Yang, "Synthesis and characterization of uniform arrays of copper sulphide (Cu_2S) nanorods coated with nano-layers of polypyrrole", *Langmuir*, vol. 19, pp. 4420-4426, 2003.
4. X.G. Wen and S.H. Yang, "Cu_2S/Au core/sheath nanowires prepared by a simple redox deposition method", *Nano Letters*, vol. 2, pp. 451-454, 2002.
5. X.G. Wen, W.X. Zhang, and S.H. Yang, "Solution phase synthesis of $Cu(OH)_2$ nanoribbons by coordination self-assembly using Cu_2S nanowires as precursors", *Nano Letters*, vol. 2, pp. 1397-1401, 2002.
6. Y. Nakamura, H. Yoshioka, M. Miyayama, and H. Yanagida, "Selective CO gas sensing mechanism with CuO/ZnO heterocontact", *J. Electrochem. Soc.*, vol. 137, pp. 940-943, 1990.
7. K.D. Mitzner, J. Steinhagen, and D.W. Galipeau, "Development of a micromachined hazardous gas sensor array", *Sensors and Actuators B*, vol. 93, pp. 92-99, 2003.
8. H. Nanto, T. Minami, and S. Takata, "Zinc-oxide thin-film ammonia gas sensors with high sensitivity and excellent selectivity", *J. Appl. Phys.*, vol. 60, pp. 482-484, 1986.
9. G. Sberveglieri, S. Groppelli, P. Nelli, A. Tintinelli, and G. Giunta,, "A novel method for the preparation of NH_3 sensors based on ZnO-In thin-films", *Sensors and Actuators B*, vol. 24-25, pp. 588-590, 1995.
10. N. Nakashima, M. Sakai, H. Murakami, T. Sagara, T. Wakahara, and T. Akasaka, "Construction of a metallofullerene La@C_{82}/artificial lipid film-modified electrode device and its electron transfer", *J. Phys. Chem. B*, vol. 106, pp. 3523-3525, 2002.
11. C. Jehoulet, A.J. Bard, and F. Wudl, "Electrochemical reduction and oxidation of C_{60} films", *J. Am. Chem. Soc.*, vol. 113, pp. 5456-5457, 1991.
12. W.Y. Kob, D. Dubois, W. Kutner, M.T. Jones, and K.M. Kadish, "Electrosynthesis and electrodoping of C_{60}^{n-} (n = 0, 1, 2, or 3) films - Electrochemical quartz-crystal microbalance study in acetonitrile solutions of alkali-metal, alkaline-earth-metal, and tetra-n-butylammonium cations", *J. Phys. Chem.*, vol. 97, pp. 6871-6879, 1993.
13. J. Chlistunoff, D. Cliffel, and A.J. Bard, "Electrochemistry of fullerene films", *Thin Solid Film*, vol. 257, pp. 166-184, 1995.
14. C. Jehoulet, Y.S. Obeng, Y.T. Kim, F.M. Zhou, and A.J. Bard, "Electrochemistry and langmuir trough studies of C_{60} and C_{70} films", *J. Am. Chem. Soc.*, vol. 114, pp. 4237-4247, 1992.
15. G. Tourillon and F. Garnier, "New electrochemically generated organic conducting polymers", *J. Electroanal. Chem.*, vol. 135, pp. 173-178, 1982.
16. L.Z. Fan, S.F. Yang, and S.H. Yang, "Electrochemistry of metallofullerene films: The major isomer of Dy@C_{82}", *Chem. Eur. J.*, vol. 9, pp. 5610-5617, 2003.
17. A. Kotyk, K. Janacek, and J. Koryta, *Biophysical Chemistry of Membrane Function*, Wiley, Chichester, 1988.
18. A.E.F. Nassar, J.M. Bobbitt, J.D. Stuart, and J.F. Rusling, "Catalytic reduction of organohalide pollutants by myoglobin in a biomembrane-like surfactant film", *J. Am. Chem. Soc.*, vol. 117, pp. 10986-10993, 1995.
19. J.F. Rusling and A.E.F. Nassar, "Enhanced electron-transfer for myoglobin in surfactant films on electrodes", *J. Am. Chem. Soc.*, vol. 115, pp. 11891-11897, 1993.
20. N.F. Hu and J.F. Rusling, "Electrochemistry and catalysis with myoglobin in hydrated poly(ester sulfonic acid) ionomer films", *Langmuir*, vol. 13, pp. 4119-4125, 1997.
21. L.W. Wang and N.F. Hu, "Electrochemistry and electrocatalysis with myoglobin in biomembrane-like DHP-PDDA polyelectrolyte-surfactant complex films", *J. Colloid Interface Sci.*, vol. 236, pp. 166-172, 2001.